AAS 19-696

HIGH-ENERGY LUNAR CAPTURE VIA LOW-THRUST DYNAMICAL STRUCTURES

Andrew D. Cox*, Kathleen C. Howell† and David C. Folta‡

Current and future spacecraft will leverage low-thrust propulsion to navigate from high-energy transfer trajectories to low-energy orbits near the Moon. Due to the long burn durations required for such energy changes, identifying suitable low-thrust arcs remains a design challenge. Periapse maps are employed to explore the dynamics of low-thrust, energy-optimal arcs in the lunar vicinity. Dynamical structures that separate transit and captured motion on these maps are identified and leveraged to construct preliminary low-thrust trajectory designs.

INTRODUCTION

An increasing number of spacecraft plan to leverage low-thrust propulsion systems to enable transfers to the Moon. For example, current designs for the Deep Space Gateway rely on low-thrust propulsion to deliver supplies from the Earth to a proposed habitat in a near rectilinear halo orbit near the Moon.[1] Additionally, a number of small satellites, including LunaH-Map[2] and Lunar IceCube,[3] will be launched as secondary payloads with the Exploration Mission 1 (EM-1) spacecraft, each leveraging small forces delivered by low-thrust propulsion or solar sails to adjust course and arrive in low-energy orbits around the Moon. One of the key challenges in designing a trajectory to deliver these small satellites to low-lunar orbit is reducing the spacecraft energy. As secondary payloads, the orbital energy for each satellite may only be adjusted after deployment from the primary vehicle. Without adjustments, the satellites may depart the Earth-Moon vicinity, prohibiting return to the Moon. A second challenge for these spacecraft is the large amount of uncertainty associated with the deployment state. Accordingly, a robust strategy to deliver the spacecraft to the Moon is desired.

To mitigate the challenges in the trajectory design process for spacecraft like Lunar IceCube or Lunar H-Map, dynamical structures from the Earth-Moon circular restricted three-body problem (CR3BP) and structures from the CR3BP augmented with low-thrust (CR3BP+LT) are employed. It is well-established that the CR3BP invariant manifolds associated with planar periodic orbits located in the forbidden region gateways act as separatrices between transit and non-transit motion at the the gateway.[4] Thus, by selecting trajectory arcs that pass within the manifold boundaries, transfers that navigate through the L_1 or L_2 gateways to reach the Moon are straightforwardly designed.[5,6] Low-thrust has previously been applied to these ballistic transfers to achieve a final state near the Moon; optimization methods are also utilized to identify a suitable low-thrust control history.[7,8] However, these approaches typically apply to low-energy spacecraft paths without

*Ph.D. Candidate, School of Aeronautics and Astronautics, Purdue University, West Lafayette, IN 47907; cox50@purdue.edu

†Hsu Lo Distinguished Professor of Aeronautics and Astronautics, School of Aeronautics and Astronautics, Purdue University, West Lafayette, IN 47907; howell@purdue.edu

‡Senior Fellow, NASA Goddard Space Flight Center, Greenbelt, MD, 20771; david.c.folta@nasa.gov

large energy changes. One strategy to accomplish a sizable energy change via low thrust is a low-thrust spiral;[9] by combining spiraling motion with other structures, end-to-end transfers may be designed.[10,11,12] This investigation supplies new insights to guide high-energy lunar capture by applying Poincaré mapping strategies. In particular, apses along low-thrust spiral trajectories near the Moon are explored and linked to other ballistic and low-thrust paths to supply preliminary trajectory designs and control histories.

BACKGROUND

The first step in computing and leveraging dynamical structures within the CR3BP and the CR3BP+LT is the development of the dynamical models. An energy-based approach is employed to derive the governing equations in the CR3BP and produce an expression for the natural Hamiltonian. By augmenting the CR3BP equations of motion (EOMs) with a low-thrust term, the CR3BP+LT is constructed. Finally, invariant manifolds associated with periodic orbits and apse maps are introduced as structures to be leveraged for this analysis.

Circular Restricted 3-Body Problem

The CR3BP describes the motion of a relatively small body, such as a spacecraft, in the presence of two larger gravitational point masses (P_1 and P_2) with paths that evolve along circular orbits about their mutual barycenter (B). To simplify the governing equations and enable straightforward visualization of periodic solutions, the motion of the spacecraft is described in a right-handed frame ($\hat{x},\ \hat{y},\ \hat{z}$) that rotates with the two primaries, as seen in Figure 1, where $\hat{x}$, $\hat{y}$, and $\hat{z}$ are vectors of unit length. The system is parameterized by the mass ratio, $\mu = M_2/(M_1+M_2)$, where M_1 and M_2

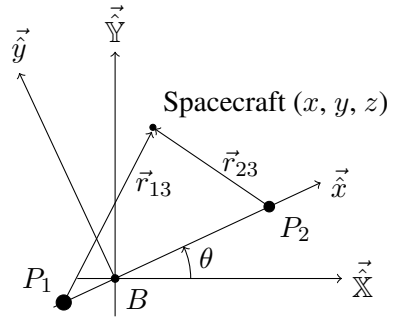

Figure 1: CR3BP system configuration

are the masses of the primaries and $M_1 \geq M_2$. To facilitate numerical integration, the dimensional values are nondimensionalized by characteristic quantities such that the distance between P_1 and P_2 is unity, the mean motion of the two primaries is unity, and the masses of each body range from zero to one.[13] The spacecraft is located relative to the system barycenter in the rotating frame via the vector $\vec{r} = \{x\ \ y\ \ z\}^T$.

The equations of motion governing the CR3BP are derived via a Hamiltonian energy approach. Let the *natural Hamiltonian* be expressed as

$$H_{nat} = \frac{1}{2}v^2 - \frac{1}{2}\left(x^2 + y^2\right) - \frac{1-\mu}{r_{13}} - \frac{\mu}{r_{23}}\,, \tag{1}$$

where r_{13} and r_{23} are the distances between the spacecraft (P_3) and the two primaries,

$$r_{13} = \sqrt{(x+\mu)^2 + y^2 + z^2}\,, \qquad r_{23} = \sqrt{(x-1+\mu)^2 + y^2 + z^2}\,,$$

and v is the magnitude of the rotating velocity vector, $v^2 = \dot{x}^2 + \dot{y}^2 + \dot{z}^2$. By applying Hamilton's canonical equations of motion, a set of differential equations that govern the motion of P_3 emerges,

$$\ddot{x} = 2\dot{y} + \Omega_x, \tag{2}$$

$$\ddot{y} = -2\dot{x} + \Omega_y, \tag{3}$$

$$\ddot{z} = \Omega_z, \tag{4}$$

where Ω is the CR3BP *pseudo-potential* function,

$$\Omega = \frac{1}{2}(x^2 + y^2) + \frac{1-\mu}{r_{13}} + \frac{\mu}{r_{23}}\,, \tag{5}$$

and Ω_x, Ω_y, and Ω_z represent the partial derivative of Ω with respect to the subscripted state variables x, y, and z, respectively. Because the CR3BP is autonomous and conservative, H_{nat} is constant and proportional to the *Jacobi constant*, $C = -2H_{nat}$, commonly leveraged as a measure of the energy associated with arcs in the CR3BP.

CR3BP Incorporating Low-Thrust

To incorporate low-thrust into the CR3BP, the low-thrust acceleration vector is first defined. This vector,

$$\vec{a}_{lt} = a_{lt}\hat{u}\,, \tag{6}$$

is oriented relative to the rotating frame via the unit vector $\hat{u}$ and scaled by the nondimensional acceleration magnitude, $a_{lt} = f/m$. In this expression, f represents the nondimensional thrust magnitude and m is the nondimensional spacecraft mass, $m = M_3/M_{3,0}$, where M_3 is the instantaneous spacecraft mass and $M_{3,0}$ is the initial (wet) spacecraft mass. In the Earth-Moon CR3BP+LT, f values on the order of 1e-2 are representative of current technological capabilities, as listed in Table 1. When this additional acceleration is incorporated into the CR3BP dynamics, the equations

Table 1: Low-Thrust Spacecraft Parameters

Spacecraft	$M_{3,0}$ kg	F mN	a_{lt} m/s^2	f (Earth-Moon) nondim
Deep Space 1 [14]	486	92.0	1.893e-4	6.95e-2
Hayabusa [15]	510	24.0	4.706e-5	1.73e-2
Dawn [16]	1218	92.7	7.611e-5	2.79e-2
Lunar IceCube [3]	14	1.15	8.214e-5	3.01e-2

of motion become

$$\ddot{x} = 2\dot{y} + \Omega_x + a_{lt}u_x, \tag{7}$$

$$\ddot{y} = -2\dot{x} + \Omega_y + a_{lt}u_y, \tag{8}$$

$$\ddot{z} = \Omega_z + a_{lt}u_z, \tag{9}$$

$$\dot{m} = \frac{-fl_*}{I_{sp}g_0t_*}, \tag{10}$$

where u_x, u_y, and u_z are the individual components of $\hat{u}$ along each of the rotating axes, l_* and t_* are the characteristic length and time quantities that nondimensionalize the CR3BP+LT coordinates, I_{sp} is the specific impulse associated with the propulsion system, and $g_0 = 9.80665\text{e-}3$ km/s^2.

In general, the natural Hamiltonian is not constant in the CR3BP+LT. The scalar time derivative, $\dot{H}_{nat}$, is related to the low-thrust acceleration via the relationship,

$$\dot{H}_{nat} = \vec{v} \cdot \vec{a}_{lt}, \tag{11}$$

where $\vec{v}$ is the spacecraft velocity as observed in the rotating frame.[17] This rate is extremized when the two vectors are parallel, i.e., the natural Hamiltonian changes most rapidly when the thrust is aligned with the velocity (or anti-velocity) vector. Because this "energy-optimal" control strategy yields a non-autonomous system, few insights exist to guide design efforts for trajectories that employ such a technique. To mitigate a lack of understanding, this investigation explores the dynamics of the CR3BP+LT with the energy-optimal thrust. The analyses are restricted to the planar dynamics ($z = \dot{z} = 0 \; \forall \; t$) to facilitate visualization and to clarify the complex dynamics.

Invariant Manifolds

Although the CR3BP is largely characterized by chaotic motion, several useful structures, including periodic orbits and the associated invariant manifolds, supply order and are frequently leveraged in trajectory design applications.[18] In the planar problem, these manifolds act as separatrices and, when combined with the forbidden regions, isolate trajectories that pass between the two primaries from trajectories that remain bounded near one of the primaries (or that remain exterior to the system as whole).[4]

Apse Maps

When the properties of periodic orbits and their manifolds are unavailable (either because they are unknown, or because the system is non-autonomous), *Poincaré maps* may be employed to explore the system. A map includes three key components: a set of initial conditions, $\left\{ \vec{q}_{i,0}, \; i = 1, 2, \ldots n \right\}$, a hyperplane, Σ, and a visualization strategy. The initial conditions are numerically integrated to the hyperplane for p returns, yielding the mapping, $\mathbb{M}_{\Sigma}^{p}(\vec{q}_{i,0})$. In many applications the hyperplane is a geometric plane, e.g., a plane at some x, y, or z value, but Σ may also be a non-geometric plane. For example, *apse maps* are employed in this investigation to visualize flow patterns near the Moon. An apse is a point where the relative velocity between the spacecraft and a primary body is zero, i.e., a point such that

$$\dot{r}_{k3} = (\vec{r} - \vec{r}_k) \cdot (\vec{v} - \vec{v}_k) = 0, \tag{12}$$

where $\vec{r}_k$ and $\vec{v}_k$ are the position and velocity of the k^{th} primary body in the rotating frame. For lunar capture applications, apses relative to P_2 (i.e., the Moon in the Earth-Moon) system are of particular interest; the initial states are selected near the Moon, where each initial state is a planar apse with respect to the Moon at a specific H_{nat} value. Because these initial states all satisfy Equation (12) and are all characterized by the same H_{nat} value, the four-dimensional planar problem is reduced to two dimensions, enabling straightforward visualization of the complete dynamics (i.e., the full 4D state is recovered from a 2D representation). One common visualization strategy for apse maps is to color the initial apse states by the behavior of the resulting arc, as illustrated in Figure 2. The initial state for a trajectory that impacts the Moon (i.e., that reaches a position within the physical lunar radius) at or prior to the $p = 2$ map returns is colored orange, while the initial states for

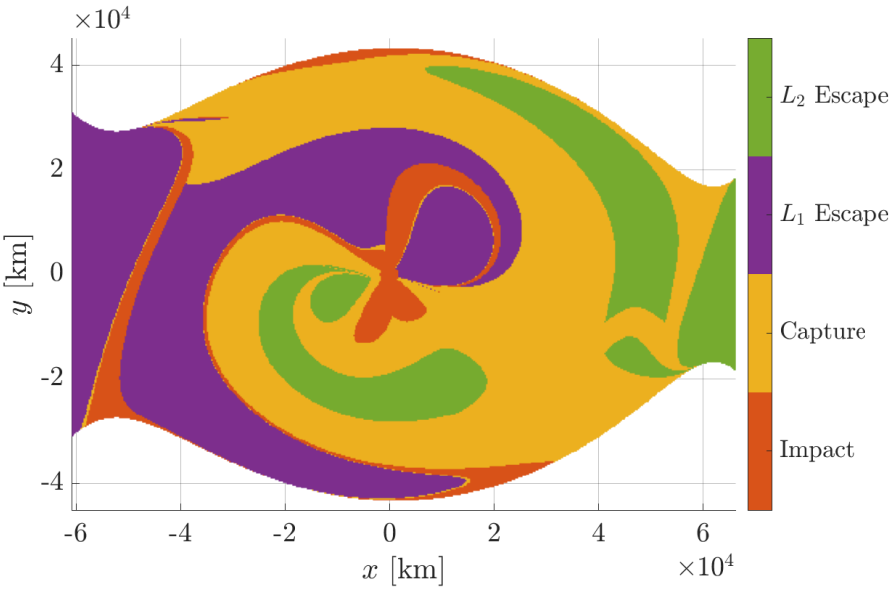

Figure 2: A ballistic lunar apse map at $H_{nat} = -1.584$ for $p = 2$ map returns in Moon-centered rotating coordinates.

trajectories that depart through the L_1 and L_2 gateways are colored purple and green. Trajectories that remain in the lunar region ($r_{23} < 115,500$ km) are termed "captured," and the associated initial states are depicted in yellow. Clear structures, i.e., colored lobes, are visible in the map; these structures can be linked to other known structures in the CR3BP. For example, the invariant manifolds associated with the L_1 and L_2 Lyapunov orbits at the same H_{nat} value bound the L_1 and L_2 escape regions.[19,20,21] Accordingly, an apse map with this visualization scheme supplies useful information for capture applications. A spacecraft entering the lunar region may target an apse in one of the capture regions to remain near the Moon for at least p map returns; if an apse along the incoming trajectory is located in one of the escape regions, the spacecraft will depart within p map returns.

LOW-THRUST APSE MAPS

Apse maps may also be employed in the CR3BP+LT with anti-velocity-pointing thrust to explore options for lunar capture. The map is constructed in the same way as the ballistic map: a set of apses near the Moon, all at a consistent H_{nat} value, are propagated for p returns to the apse hyperplane and colored by the fate of the resulting trajectory. When the thrust magnitude is very small, as in Figure 3(a), the low-thrust apse maps appear very similar to the ballistic maps. However, as the thrust magnitude increases, the structures on the map change, as illustrated in Figure 3(b). For example, the low-thrust apse map for $f = 3$e-2 (consistent with the capabilities of Lunar IceCube) retains a teardrop-shaped lobe of L_1 escape motion near the center of the map, as well as some L_1 and L_2 escape regions on the left and ride sides of the plot. However, there is significantly less escape motion in the center of the plot; instead, many more options for capture exist. Because the propagation is implemented with anti-velocity-pointing thrust, a strategy to decrease H_{nat}, it is not surprising that fewer arcs escape during the two map returns. As the energy decreases, the L_1 and

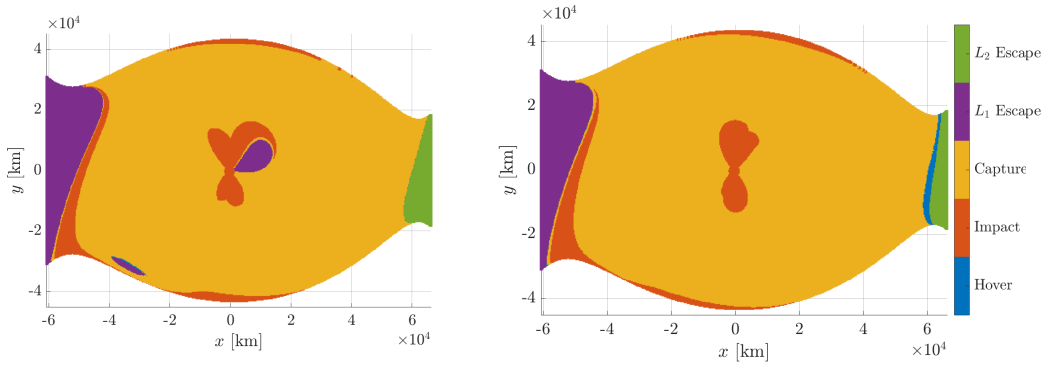

(a) Lunar IceCube Capability: $f = 3\text{e-}2$

(b) Deep Space 1 Capability: $f = 7\text{e-}2$

Figure 3: Low-thrust lunar apse maps for $H_{nat} = -1.584$ and $p = 2$ in Moon-centered rotating coordinates. The initial states are propagated with anti-velocity-pointing thrust with $I_{sp} = 2500$ seconds.

L_2 gateways close, prohibiting transit from the lunar region. At a larger thrust magnitude of $f = 7\text{e-}2$ (a Deep Space 1 capability), the apse map, plotted in Figure 3(b) includes even more opportunities for capture. While the boundaries of these regions are defined by the L_1 and L_2 Lyapunov manifolds in the ballistic problem, no such structures are known to bound the regions on the low-thrust apse maps. Because the thrust orientation, $\hat{a}_{lt}$, is aligned with the evolving anti-velocity vector, the CR3BP+LT is nonautonomous, does not admit an integral of the motion, and includes no periodic solutions. Accordingly, the low-thrust apse maps must be constructed by propagating each of the initial conditions to determine its fate.

The low-thrust maps include a new type of behavior, colored blue and termed "hover" motion, that is not present in the ballistic map. These initial states yield trajectories that, when propagated with anti-velocity-pointing thrust, eventually reach a velocity magnitude of zero. Due to the implementation of the control law, as the velocity magnitude approaches zero (numerically equivalent to 2^{-52} nondimensional units, or about 2.27e-16 km/s in the Earth-Moon system), as in Figure 4(b), the orientation of the velocity vector is poorly defined, oscillating with numerical noise as well as the with spacecraft motion. Accordingly, the hover is accomplished by rapidly reorienting the low-thrust acceleration vector, an impractical control method in practice.

Despite the practical difficulty of accomplishing a hover maneuver, the associated map regions supply insights for trajectory design. In the maps depicted in Figure 3, the initial states that yield hover motion are located on several of the boundaries between states linked to captured motion and states associated with L_1 or L_2 escape. A sample of the trajectories initiated from these states, plotted in Figure 4, illustrate the differences between the regions. The initial states for the five sample arcs are selected in a horizontal line at $y = 16,384.6$ km spanning the blue hover region near $x = 6 \times 10^4$ km in Figure 3(b). (A similar band of hover motion is included in the map for $f = 3\text{e-}2$ at the boundary between capture and L_2 escape motion in the L_2 gateway.) The arcs, plotted in position space in Figure 4(a), initially flow along the $-\hat{y}$ direction toward L_2 and toward a set of low-thrust equilibria, termed a *zero acceleration contour* (ZAC), plotted in gray. The ZAC is a set of points that satisfy the equation $\vec{\nabla}\Omega = \vec{0}$ with $f = 7\text{e-}2$, each point associated with a unique orientation of $\hat{u}$.[17] One intuitive hypothesis to explain the hover motion is that the arcs reach

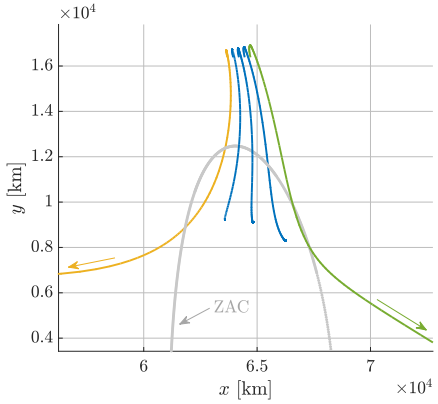

(a) Moon-centered Earth-Moon rotating frame with the low-thrust zero acceleration contours (ZACs) for reference

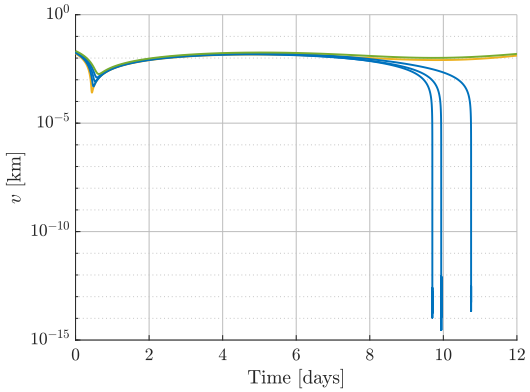

(b) The hover arcs reach a velocity magnitude of zero

Figure 4: Sample arcs from the low-thrust apse map in Figure 3(b); the "hover" arcs (blue) reach a zero velocity magnitude in the vicinity of the ZAC

one of these equilibria states. However, because $\hat{u}$ changes continuously with the orientation of $\vec{v}$ when the velocity-pointing control law is employed, no single point on the ZAC is associated with a trajectory; during the hover maneuvers (located at the ends of the blue arcs), the location of the instantaneous low-thrust equilibrium solution changes as rapidly as the orientation of $\hat{u}$. Accordingly, the hover arcs do not intersect an equilibrium point. In fact, the locations where the arcs reach $v = 0$ are unrelated to the ZAC. Instead, the hover locations are the points where the forbidden regions "catch up" with the low-thrust trajectory. Recall that H_{nat} decreases monotonically when the anti-velocity-pointing control law is applied; thus, as the trajectories evolve from the initial states on the apse map, the forbidden regions grow, increasingly restricting the motion of the spacecraft. At the hover locations, the boundary of a forbidden region, a *zero velocity contour*,[13] intersects with the trajectory, leaving the space "in front" of the hover location (i.e., in the direction of the trajectory evolution prior to the hover) accessible but the area "behind" the hover location inaccessible. Having reached a lower H_{nat} value, an alternative control technique (a velocity-aligned direction is undefined) may be employed to further influence the trajectory evolution. Indeed, the low-thrust acceleration is particularly influential on the spacecraft path due to the low velocity magnitude at these points. Thus, the map states associated with hover motion are candidates for further study.

HIGH-ENERGY CAPTURE STRATEGIES

Two strategies to design high-energy, low-thrust lunar capture trajectories are explored. The first scheme leverages a low-thrust apse map to identify points in the lunar region at a high H_{nat} value that result in captured motion. The second technique augments an L_2 Lyapunov manifold with low-thrust to decrease the H_{nat} value along the trajectory before arriving in the lunar region, where a similar (but lower energy) low-thrust apse map is employed to identify capture options. In both strategies, the low-thrust force is aligned with the anti-velocity direction to supply the maximum H_{nat} rate of change.

Lunar IceCube

The Lunar IceCube trajectory is referenced as a source of realistic parameters to illustrate the proposed design strategies. Lunar IceCube (LIC), a 14 kilogram, 6U "cubesat", is equipped with a low-thrust propulsion system that can deliver up to 1.15 millinewtons ($f \approx$ 3e-2 in the Earth-Moon CR3BP+LT) of force with a specific impulse, or I_{sp}, of 2500 seconds.[3] About 5 days after deployment from EM-1, LIC flies past the Moon, as illustrated in Figure 5, and the subsequent trajectory extends far from the Earth and Moon. A little less than six months later, the spacecraft

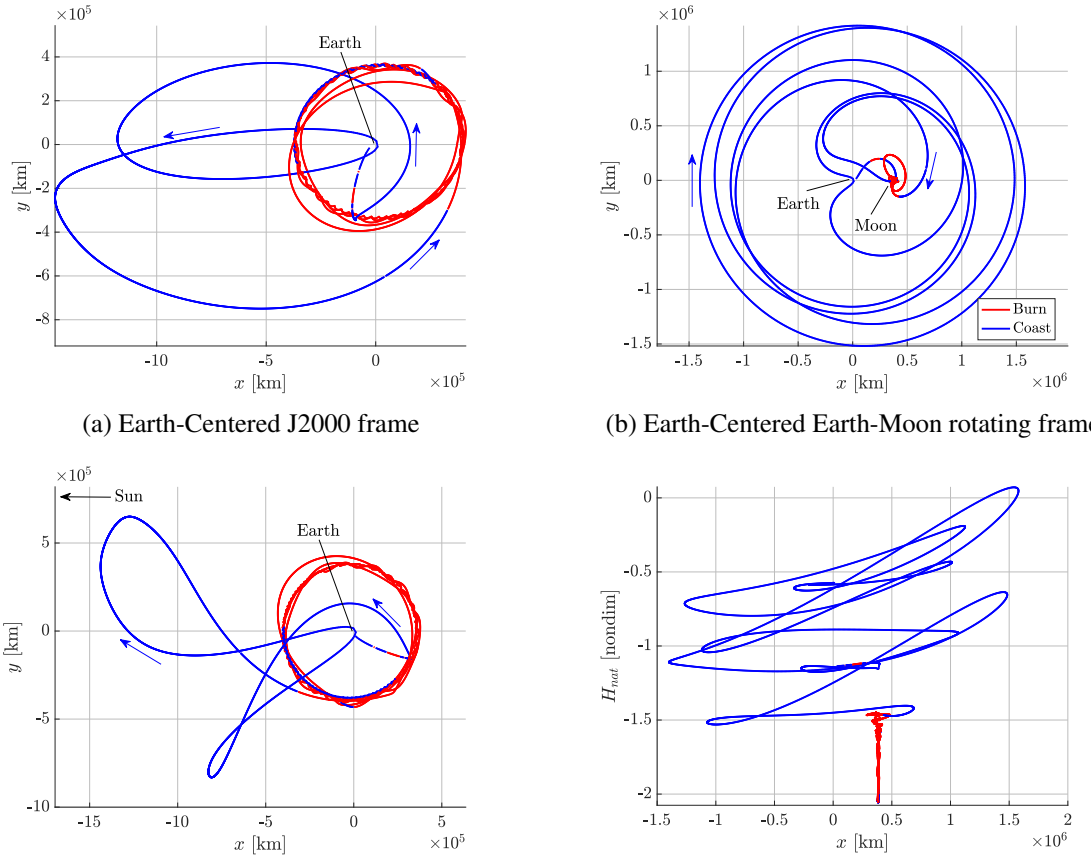

(a) Earth-Centered J2000 frame

(b) Earth-Centered Earth-Moon rotating frame

(c) Earth-Centered Sun-Earth rotating frame

(d) Earth-Centered Earth-Moon rotating frame

Figure 5: Planar projections of a LIC trajectory option in a variety of reference frames; blue arcs represent ballistic (coasting) motion, while red arcs indicate that the low-thrust engine is active (burning). This baseline solution begins at a deployment epoch of June 27, 2020 at 21:08:03 UTC, and ends in a low-lunar orbit on May 22, 2021.

returns to the Moon and employs the low-thrust propulsion system to decrease the orbital energy and capture into a polar lunar orbit. For the current analysis, only the final approach to the Moon and the subsequent energy decrease and capture are considered. During this final phase, the H_{nat} value in the Earth-Moon rotating frame remains between -1.53 and -1.4; the Hamiltonian fluctuates because the trajectory is propagated in an ephemeris model in which H_{nat} is not an integral of the motion. Accordingly, H_{nat} values in this range are employed as reasonable values to illustrate the proposed capture strategies. Additionally, while the trajectory does include several small thrusting

arcs prior to the long, final burn, the mass change is negligible (0.011 kg of the 14 kg wet mass), thus, the initial mass for all capture strategies is set to 100%.

Capture Initiated Near the Moon

One strategy for high-energy capture initiates thrusting in the anti-velocity direction when the spacecraft arrives in the vicinity of the Moon, as illustrated by the Lunar IceCube (LIC) trajectory in Figure 5. Clearly, capture near the Moon is accomplished in this specific scenario, but the single LIC trajectory does not supply information about other nearby solutions. For a more general view of capture opportunities in the lunar region, an apse map is constructed. Consistent with the LIC trajectory, the set of initial states is characterized by an H_{nat} value of -1.425, and the propagation is modeled with an I_{sp} value of 2500 seconds. Two thrust magnitudes are employed: the LIC thrust capability of $f = 3\text{e-}2$, and a larger thrust magnitude of $f = 7\text{e-}2$, consistent with a Deep Space 1 capability. To explore capture options, each point on the map is propagated for up to 20 map returns (i.e., apses), and the initial conditions are colored by the fate of the associated trajectory, consistent with the scheme in Figure 2. The resulting maps, plotted in Figure 6, are dominated by escaping trajectories. The lack of other types of motion is not surprising given the high energy

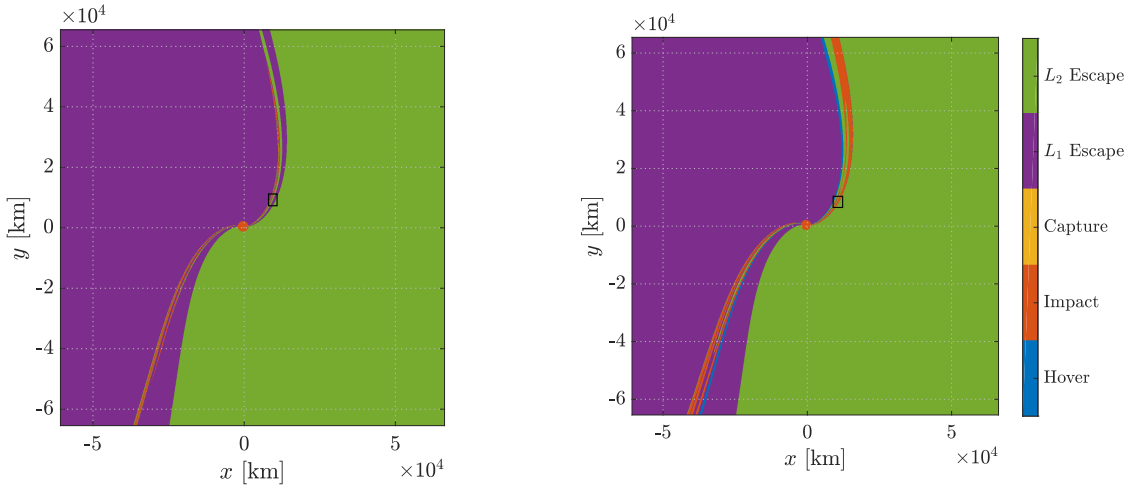

(a) Lunar IceCube Capability: $f = 3\text{e-}2$

(b) Deep Space 1 Capability: $f = 7\text{e-}2$

Figure 6: Apse maps in the Moon-centered Earth-Moon rotating frame for $H_{nat} = -1.425$, $I_{sp} = 2500$ seconds, and $p = 20$ map returns.

and small thrust force; at energies this high, the low-thrust propulsion is generally not sufficient to prevent the spacecraft from departing the lunar region. (For these high energy maps, departure is defined by the radius $r_{23} > 385,000$ km.) However, thin bands of more nuanced behavior appear in the maps between the large regions of L_1 and L_2 escapes. Zooming in on the structures within the black boxes in Figure 6, as depicted in Figure 7, reveals even thinner bands of initial conditions with different fates. At the resolution available in these maps, no capture options are revealed for the LIC thrust capability. This result does not necessarily preclude capture at this energy and thrust capability; a modified thrust strategy may adjust some of the collision arcs to achieve capture. When a larger thrust magnitude is employed, as in Figure 7(b), capture opportunities become available. These apses, colored yellow on the map, correspond to arcs that pass through 20 apses without

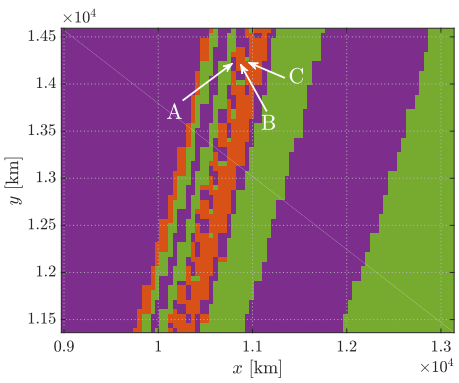

(a) Lunar IceCube Capability: $f = 3\text{e-}2$

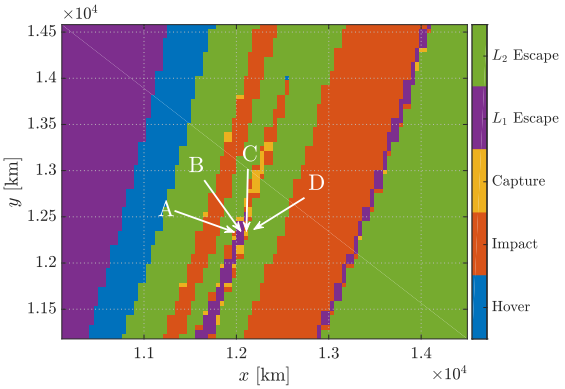

(b) Deep Space 1 Capability: $f = 7\text{e-}2$

Figure 7: Close-up views of the apse map regions marked by black squares in Figure 6 reveal chaotic motion; Moon-centered Earth-Moon rotating frame

colliding with the Moon or departing the lunar region. Although capture opportunities are apparent at the higher thrust capability, they are generally isolated and located on the boundaries between bands of other behaviors, in contrast with the dense bands of L_1 escape, L_2 escape, and impact motion. Indeed, one of the defining characteristics of the high-energy apse maps in Figures 6 and 7 is *chaos*: initial states at apses located close together frequently yield very different arcs, particularly in the thin bands viewed in Figure 7. Selecting several points in this regions with impact and capture motion, as labeled in Figure 7, and plotting the associated trajectories, visualized in Figure 8, illustrates the chaotic nature of the dynamics. For each set of arcs, the initial conditions are

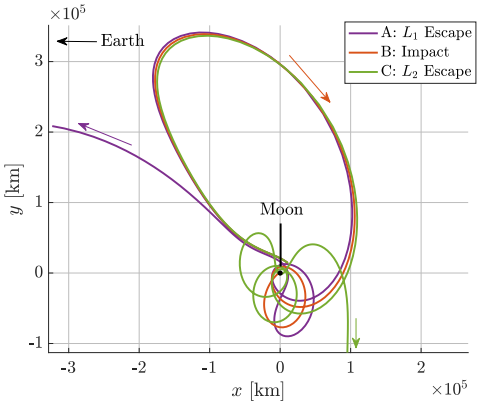

(a) Lunar IceCube Capability: $f = 3\text{e-}2$

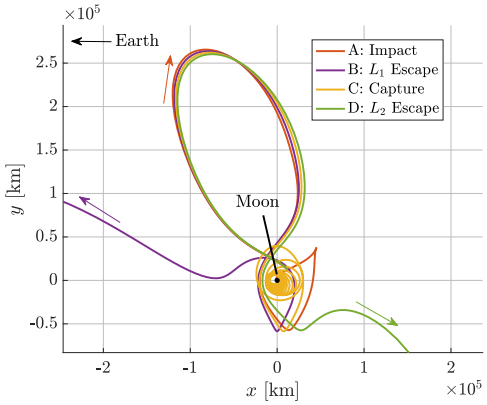

(b) Deep Space 1 Capability: $f = 7\text{e-}2$

Figure 8: The arcs associated with the points labeled in Figure 7 illustrate the chaotic nature of the dynamics; Moon-centered Earth-Moon rotating frame

located at a consistent y-coordinate, and are separated by an x distance of less than 39 kilometers (the velocity magnitude is a function of the H_{nat} value and the velocity direction is orthogonal to the $\vec{r}_{23}$ vector). Despite the similar initial states, the evolution of each trajectory varies significantly.

Although no capture opportunities are apparent for the LIC thrust magnitude of $f = 3\text{e-}2$, the

geometries of the arcs represented by the map are similar to the LIC ephemeris solution. For example, the large lobe common to the arcs in Figure 8(a) is very similar to the LIC trajectory at the beginning of the thrust arc that delivers the spacecraft to lunar orbit, plotted in Figure 5(b). These similarities, as well as first-hand knowledge of the difficulties associated with designing the LIC trajectory, suggest that the chaos observed in the this planar apse map is consistent with the spatial ephemeris model.

For either of the thrust levels, opportunities for capture exist only in the thin, chaotic bands. Accordingly, a design strategy that initiates the capture burn near the Moon is likely to be sensitive, diverging from the desired behavior when small perturbations are encountered. This sensitivity affects not only the design process, but has implications for operations as well. Any failure in the propulsion or navigation systems are likely to effect large changes on the trajectory and may place the spacecraft on a path that does not capture near the Moon, effectively ending a cubesat mission like Lunar IceCube or LunaH-Map.

Capture Initiated Far from the Moon

As an alternative to a strategy that initiates the capture sequence at a location near the Moon, consider a strategy that employs low thrust to decrease the H_{nat} value prior to arrival at the Moon. As illustrated in the apse maps for $H_{nat} = -1.584$, depicted in Figure 2, opportunities for capture are more abundant and less chaotic at lower energies than the high-energy results illustrated in Figure 6. In fact, a majority of the points on the low-energy map represent capture opportunities with far less sensitivity than the options at $H_{nat} = -1.425$. Accordingly, a spacecraft that enters the lunar region with an lower H_{nat} energy value is afforded more flexibility in achieving lunar capture; even if the baseline trajectory is perturbed from a specific target, the spacecraft is unlikely to rapidly depart the region.

To isolate low-thrust arcs that reach the lunar vicinity at a low energy, the invariant manifolds associated with a ballistic L_2 Lyapunov orbit are employed. In previous studies, such arrival arcs have been produced by propagating a trajectory in reverse time from a low lunar orbit to some energetic or physical hyperplane.[3] While this method reveals capture paths, it restricts the exploration to a specific destination orbit. By utilizing the separatrix property of the L_2 Lyapunov manifolds, a more general set of capture options may be constructed. The proposed capture strategy is comprised of several steps:

1. Propagate the *stable* manifold, W^{S+}, associated with an Earth-Moon L_2 Lyapunov orbit in reverse time to a hyperplane, Σ_1, that is located exterior to the L_2 gateway.

2. Propagate the stable manifold states with anti-velocity-pointing low-thrust in reverse time from Σ_1 to another hyperplane, Σ_2 that serves as an interface between a high-energy trajectory incoming to the Moon and a low-thrust arc that decreases the H_{nat} energy.

3. Construct a low-thrust apse map (anti-velocity-pointing thrust, forward time) at the same H_{nat} energy value as the L_2 Lyapunov orbit

4. Overlay the ballistic *unstable* manifold, W^{U-}, associated with the L_2 Lyapunov orbit on the low-thrust apse map and identify intersections with capture opportunities.

From a mission sequence (i.e., forward time) perspective, a spacecraft approaching the Moon first targets a state at Σ_2 "inside" $\tilde{W}_{lt}$. At Σ_2, the low-thrust propulsion is enabled with an anti-velocity-

pointing orientation and the spacecraft proceeds to Σ_1. During this propagation, the H_{nat} value along the trajectory decreases to match the energy associated with the L_2 orbit. At Σ_1, the low-thrust force is disabled and the trajectory is allowed to evolve ballistically, bounded by the L_2 Lyapunov manifold separatrix, W^{S+} and then W^{U-}. Apses on the trajectory during this ballistic evolution are plotted on the apse map and compared with the low-thrust behavior available at each apse; assuming one or more of the apses correspond to a low-thrust trajectory that captures about the Moon, the low-thrust propulsion is re-enabled at the appropriate apse to begin a low-thrust spiral into a low-energy lunar orbit.

To illustrate this sequence, parameters consistent with the LIC trajectory are again employed. Select an L_2 Lyapunov orbit with an H_{nat} value of -1.584, a low energy level that still permits transit through the L_2 gateway. The stable manifold that arrives at the orbit from the right side, W^{S+}, is propagated in reverse time to the Σ_1 hyperplane, located exterior to the system at $x = 81,422.6$ km in the Moon-centered Earth-Moon rotating frame, as depicted in Figure 9(a). At this hyperplane,

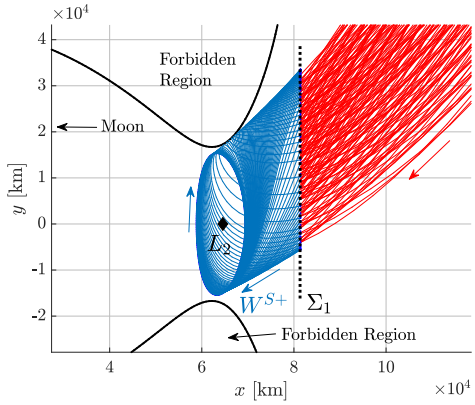

(a) The low-thrust arcs (red) flow directly into and onto the ballistic L_2 Lyapunov manifold (blue); Moon-centered Earth-Moon rotating frame. The ballistic motion is bounded by the forbidden region at $H_{nat} = -1.584$

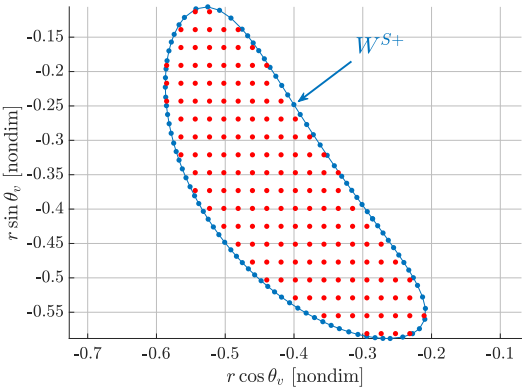

(b) Initial conditions for the low-thrust arcs are selected at Σ_1 from the interior (red points) of the ballistic manifold, and from the manifold itself (blue); tube topology at $x = 81,422.6$ km

Figure 9: At the Σ_1 hyperplane, low-thrust arcs flow into and onto the ballistic L_2 Lyapunov manifold

a tube-topology representation of the manifold is constructed,[22] consisting of a radial coordinate, $r = (y-\tilde{y})/(2\tilde{y})$, and an angular coordinate $\theta_v = \arctan(\dot{y}/\dot{x})$. For this application, $\tilde{y}$ is selected to be the y-coordinate of the nearest upper ($y < 0$) edge of the forbidden region. When plotted in polar form, as in Figure 9(b), this topology supplies a full representation of the planar states (i.e., all four Cartesian components of the state vector are available from the 2D representation). Because the full state is represented on the map, determining whether a planar trajectory exists within the manifold separatrix is straightforward - simply consider if the trajectory is encircled by the manifold contour on the map. Leveraging this technique, a set of states inside the manifold are selected (plotted as red dots in Figure 9(b)). These states are then employed as initial conditions for low-thrust arcs that are propagated in reverse time with anti-velocity-pointing thrust to the second hyperplane, Σ_2. Additionally, the manifold states (plotted in blue) are also propagated to Σ_2 with the same thrust strategy, yielding the $\tilde{W}_{lt}$ set; although these arcs appear similar to a manifold structure, they are

not mathematically related to the originating periodic orbit, nor are they manifold arcs associated with a low-thrust periodic orbit.[17]

The Σ_2 hyperplane serves as an interface between an incoming high-energy trajectory and a low-thrust arc that decreases the H_{nat} energy. To facilitate high-energy capture, Σ_2 should be sufficiently far from the low-energy W^{S+} manifold such that the energy change along the low-thrust arcs between Σ_2 and Σ_1 is large. Placing the Σ_2 hyperplane at $x = -687,871.5$ km (again in the Moon-centered Earth-Moon rotating frame), as illustrated in Figure 10(a), supplies an energy change consistent with the LIC trajectory. At this interface, a mapping strategy similar to the tube

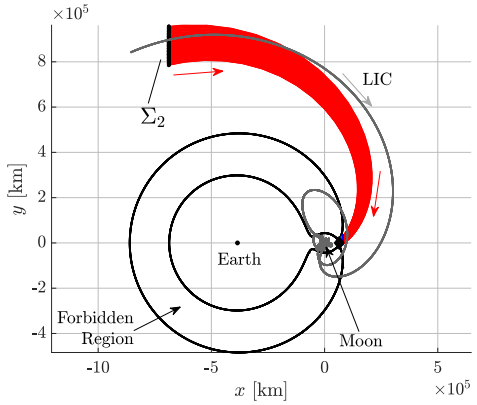

(a) The low-thrust arcs (red) originate at the Σ_2 hyperplane, and have a similar geometry to the Lunar IceCube (LIC) approach path; Moon-centered Earth-Moon rotating frame

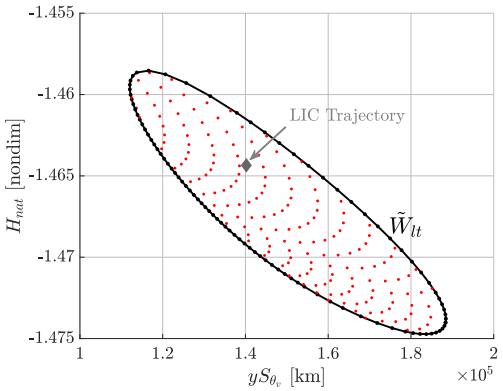

(b) A projection of the low-thrust states at Σ_2. Low-thrust arcs propagated from the stable manifold (black) completely enclose low-thrust arcs propagated from the interior of the manifold

Figure 10: Low-thrust trajectories that flow into a ballistic manifold decrease the H_{nat} value while simultaneously delivering the spacecraft to the lunar vicinity; Moon-centered Earth-Moon rotating frame

topology employed at Σ_1 is applied; the y-coordinate of the arcs replaces the scaled y-coordinate, but the velocity angle, θ_v, is identical to the previous definition. However, in contrast to the map at Σ_1, this mapping cannot represent the full state in a 2-dimensional plot due to the variations in the H_{nat} values associated with the low-thrust arcs at Σ_2. Accordingly, H_{nat} is included in the mapping, yielding a 3-dimensional surface, a projection of which appears in Figure 10(b). This mapping illustrates a similar structure: The low-thrust arcs propagated from within the ballistic manifold, plotted in red, remain within low-thrust arcs propagated from the manifold itself, $\tilde{W}_{lt}$, plotted in black. In contrast to the ballistic CR3BP, this apparent low-thrust separatrix behavior is not predicted by the dynamics, but it does persist across a variety of Σ_2 locations and a variety of H_{nat} energy values. Increasing the density of the low-thrust arcs propagated from within the ballistic manifold confirms this separatrix behavior: all of the points within $\tilde{W}_{lt}$ flow into W^{S+}.

While this analysis is conducted in the Earth-Moon CR3BP+LT, solar gravity is a non-negligible force far from the system barycenter, i.e., along the arcs that approach Σ_2. The geometry of the LIC trajectory, propagated in an Earth-Moon-Sun ephemeris model, is different than the Earth-Moon arcs despite the similarities in the states at Σ_2, as illustrated in Figure 10(b). Indeed, previous investigations note the importance of solar gravity during this approach to the Earth-Moon system.[3] However, including the Sun in the model eliminates the autonomous nature of the gravitational dy-

namics, complicating the analysis by adding an epoch-dependency. Thus, to develop the proposed capture strategy, solar gravity is omitted from the model. For mission-specific applications, a relevant epoch (or range of epochs) limits the scope of the design problem, and the low-thrust arcs may be propagated between Σ_1 and Σ_2 in the appropriate dynamical environment. Regardless of the specific model employed for the approach to Σ_1, the method remains unchanged.

Once a spacecraft has navigated through the low-thrust "tube", $\tilde{W}_{lt}$, and, subsequently, the ballistic W^{S+} manifold, the trajectory remains bounded by the L_2 Lyapunov unstable manifold that departs the orbit to the left, W^{U-}. However, the H_{nat} energy associated with the trajectory and the bounding manifold are not sufficiently low to prevent escape from the lunar region. Accordingly, additional thrusting must be incorporated to reduce the H_{nat} value, i.e., to capture about the Moon. The low-thrust apse map constructed at the same energy level as the ballistic manifold with anti-velocity-pointing thrust, plotted in Figure 11, identifies locations in the lunar region where the thruster may be re-activated to capture in a low-energy orbit about the Moon. Note that this map is

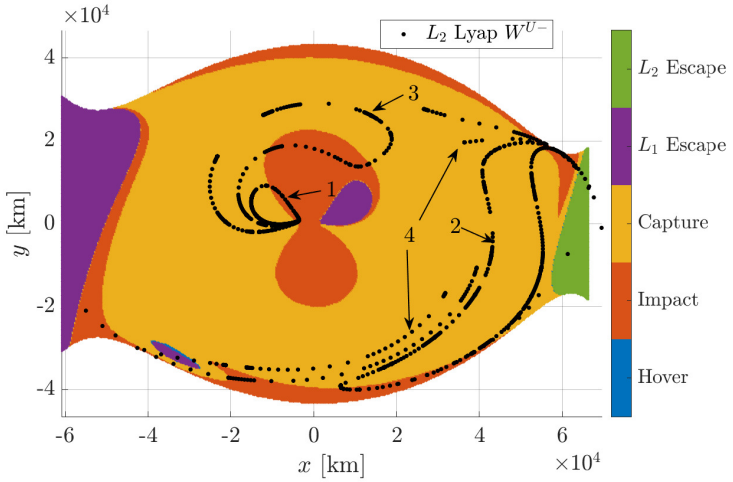

Figure 11: Ballistic L_2 Lyapunov unstable manifolds (black) overlaid on a low-thrust apse map (anti-velocity-pointing, f = 3e-2, I_{sp} = 2500 sec) for $H_{nat} = -1.584$ and $p = 20$; Moon-centered Earth-Moon rotating frame

constructed with the same parameters as the map in Figure 3(a), but this latter map is propagated to 20 apses (a sufficient amount of time for the low-thrust force to decrease the H_{nat} value such that both gateways are closed) whereas the map in Figure 3(a) is propagated to only two apses. Accordingly, the 20-return map includes all of the information available in the 2-return map; every escape and impact condition from the 2-return map is captured by the 20-return map. However, some of the initial conditions that yield capture motion for two map returns escape or impact the Moon when propagated for 20 returns. Overlaying the W^{U-} ballistic manifold apses on the map (plotted as black dots and labeled with map return number), reveals a specific subset of the capture opportunities that are accessible from within the manifold separatrix. The first and second manifold apse regions overlap almost entirely with capture opportunities; thus, nearly every arc within the L_2 Lyapunov manifold can be linked to a low-thrust path that delivers a capture trajectory. Consequently, the majority of the arcs within $\tilde{W}_{lt}$ at Σ_2 (Figure 10(b)) may be linked to a low-energy lunar orbit.

Several sample arcs are constructed to illustrate the capture process. The initial states for the arcs are located within the $\tilde{W}_{lt}$ contour at Σ_2, as depicted by the colored symbols in Figure 12(a). Each arc is propagated with anti-velocity-pointing low-thrust to Σ_1, where the thrust is disabled and

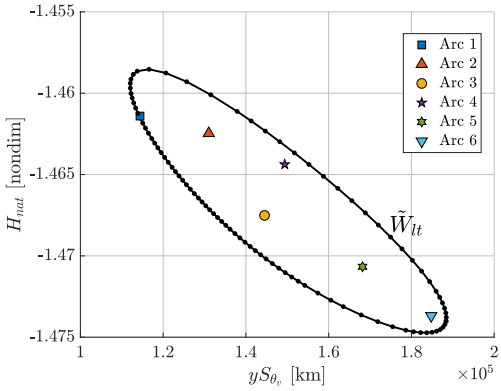

(a) Initial states for the arcs at Σ_2 within the $\tilde{W}_{lt}$ contour

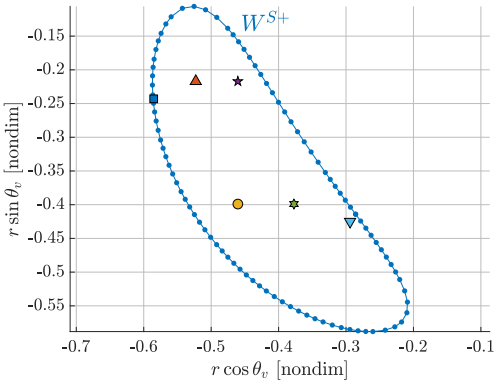

(b) Intermediate states for the arcs at Σ_1

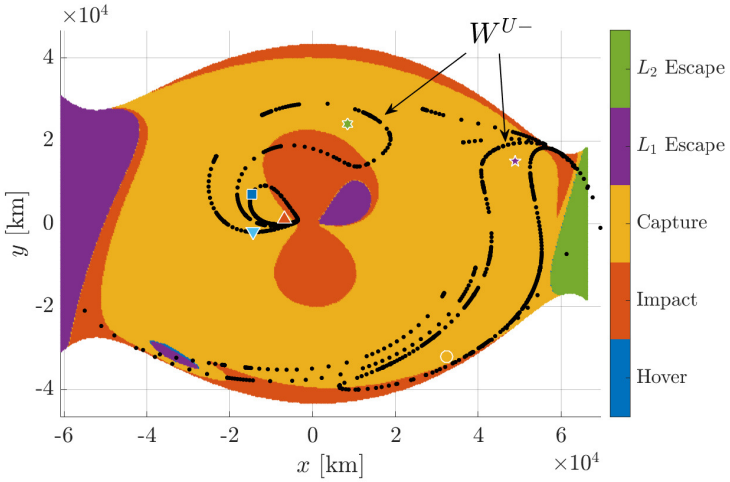

(c) Following a ballistic coast within W^{U-}, each arc re-enables the low-thrust force at an apse to capture about the Moon; Moon-centered Earth-Moon rotating frame

Figure 12: Arcs that reach a low-energy lunar orbit are designed by identifying appropriate states on the Σ_2, Σ_1, and apse maps

the arcs are allowed to evolve ballistically. The arcs coast for different time intervals: arcs 1 and 2 coast to the first apse, arcs 3 and 4 coast to the second apse, and arcs 5 and 6 coast to the third apse. As expected, these apses, plotted as colored symbols in Figure 12(c), remain within the W^{U-} separatrix. Additionally, each of these apses is located in the yellow-colored capture region on the low-thrust apse map. In contrast to the capture initiated near the Moon, the coast periods between Σ_1 and the subsequent apses provide opportunities for orbit determination and navigation updates before the second low-thrust maneuver is initiated to capture near the Moon. Additional coasting

time can be incorporated into the trajectory by directly targeting insertion onto the L_2 Lyapunov orbit, i.e., by following an arc on $\tilde{W}_{lt}$ and, equivalently, on W^{S+}, as illustrated by arc 1 in Figures 12(a) and 12(b). The initial state for arc 1, represented by a blue square, is located very near the $\tilde{W}_{lt}$ boundary at Σ_2 and remains near the W^{S+} contour at Σ_1. From the Σ_1 hyperplane, a ballistic coast along W^{S+} delivers the spacecraft to the Lyapunov orbit where an arbitrarily long coast may be included. At some later time (e.g., when a phasing constraint is satisfied), a small maneuver is sufficient to perturb the spacecraft from the periodic orbit and place it on the unstable manifold, W^{U+}, such that the spacecraft reaches the apses in Figure 12(c).

Although the six sample arcs are clearly separated on the Σ_2, Σ_1, and apse maps, the arcs follow similar paths through configuration space. The physical trajectories, plotted in Figure 13, are particularly dense as the arcs approach the Moon. The Lunar IceCube (LIC) trajectory, plotted in gray,

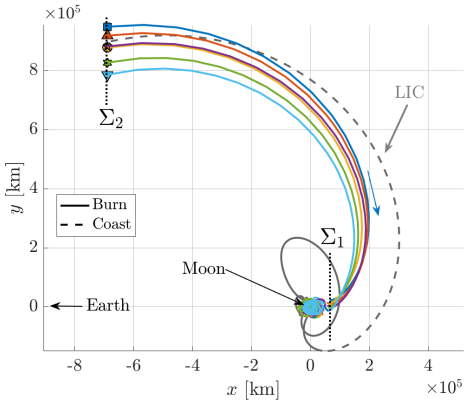

(a) Configuration space representation in the Moon-centered Earth-Moon rotating frame

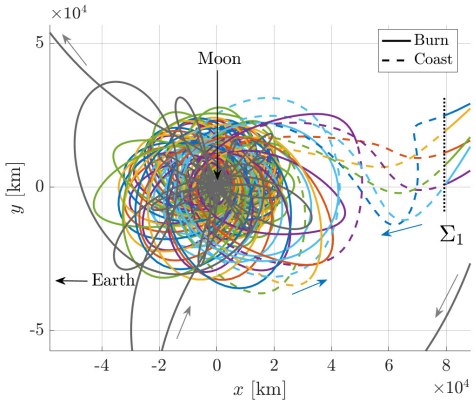

(b) A zoomed view of the lunar region

Figure 13: Sample capture trajectories in configuration space; Moon-centered Earth-Moon rotating frame

follows a similar path as the the sample arcs, but differs considerably near the Moon. Although many of these differences are a result of the different models employed to propagate the arcs (recall that the LIC trajectory is propagated in a full, spatial ephemeris model whereas the sample arcs are propagated in the planar, Earth-Moon CR3BP+LT), some of the differences are certainly due to the thrust strategy. The sample arcs employ low-thrust to decrease the H_{nat} value, constraining the approach geometry to flow through the L_2 gateway. In contrast to these sample arcs, the LIC trajectory, characterized by a much higher H_{nat} value and an initial ballistic coast, is not similarly constrained.

Another useful illustration of the capture trajectories is the H_{nat} energy evolution through time and space. The LIC trajectory, plotted in gray in Figure 14, coasts to the lunar vicinity before initiating a low-thrust maneuver to decrease energy and capture near the Moon. (Because the LIC trajectory is propagated in an ephemeris model with forces not included in the CR3BP+LT, such as solar gravity, the H_{nat} value is not constant during the coast.) In contrast, the capture arcs designed via the strategy detailed in this investigation initiate a low-thrust maneuver to decrease the H_{nat} value immediately, as is evident in the time-history plotted in Figure 14(a). A spatial representation of these planar trajectories in Figure 14(b) further illustrates the relationship between the H_{nat} value

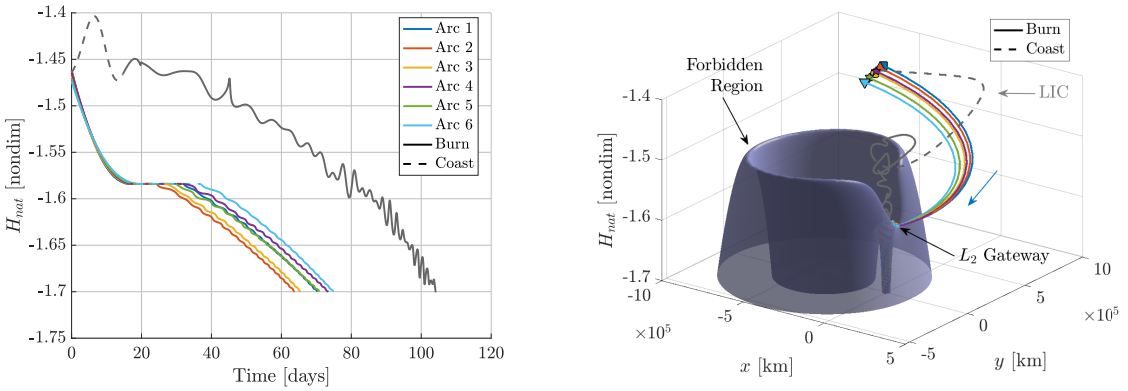

(a) Temporal representation

(b) Spatial representation

Figure 14: The H_{nat} energy along the sample arcs and the LIC trajectory decreases to a low-energy lunar orbit

along the arcs and geometry of the forbidden region. In this representation, each horizontal "slice" of the forbidden region surface is the zero velocity contour at the corresponding H_{nat} value. The planar projection of the LIC trajectory maintains a high H_{nat} value, remaining unconstrained by the forbidden region. Rather than offering flexibility, this lack of an energy constraint results in sensitivities that create design difficulties, as illustrated in the chaotic apse maps depicted in Figures 6 and 7. In contrast, the colored trajectories that employ thrusting to reduce the H_{nat} energy before arriving at the Moon pass just above the L_2 gateway and are relatively bounded near the Moon. As a result, the ballistic coast arcs that begin at Σ_1 remain captured for several returns to the apse map, bounded by W^{U-}. Thrusting may resume at any of the apses that overlap with low-thrust capture motion to further decrease the H_{nat} value along the trajectory such that escape from the lunar region is not possible, i.e., delivering the spacecraft to a low-energy lunar orbit.

CONCLUDING REMARKS

Trajectory designs that reduce the H_{nat} energy prior to arriving near the Moon benefit from reduced chaos compared to trajectories that begin energy-reducing maneuvers near the Moon. These differences between the high-energy, high-chaos dynamics and the low-energy, low-chaos dynamics are apparent when comparing energy-optimal low-thrust spirals on apse maps. Additionally, a trajectory that reaches the lunar vicinity with a relatively low H_{nat} energy may incorporate coasting segments prior to the final low-thrust maneuver, facilitating orbit determination and navigation updates. While this analysis has focused on the lunar region, the capture strategies may be generalized for capture about any secondary body in a CR3BP system. Additionally, capture via the L_1 gateway may be accomplished via similar processes. Finally, this investigation considers only the planar dynamics but may be applicable to the spatial realm. The separatrix properties of spatial manifolds are less well-established than the separatrix nature of planar manifolds, but appear to behave similarly.

ACKNOWLEDGMENTS

This work was completed at Purdue University and at the Goddard Space Flight Center in Greenbelt, Maryland. The authors wish to thank the Purdue University School of Aeronautics and As-

tronautics as well as the NASA Goddard Navigation and Mission Design branch for their facilities and support. Additionally, many thanks to the Purdue Multi-Body Dynamics Research Group for interesting discussions and ideas, with special thanks to Kenza Boudad and Robert Pritchett. This research is supported by a National Aeronautics and Space Administration (NASA) Space Technology Research Fellowship, NASA Grant NNX16AM40H.

REFERENCES

[1] M. L. McGuire, L. M. Burke, S. L. McCarty, K. J. Hack, R. J. Whitley, D. C. Davis, and C. Ocampo, "Low-Thrust Cis-Lunar Transfers Using a 40 kW-Class Solar Electric Propulsion Spacecraft," *AAS/AIAA Astrodynamics Specialist Conference*, Columbia River Gorge, Stevenson, Washington, Aug. 2017.

[2] C. Hardgrove, J. Bell, J. Thangavelautham, A. Klesh, R. Starr, T. Colaprete, M. Robinson, D. Drake, E. Johnson, and J. Christian, "The Lunar Polar Hydrogen Mapper (LunaH-Map) mission: Mapping hydrogen distributions in permanently shadowed regions of the Moon's south pole," *Annual Meeting of the Lunar Exploration Analysis Group*, Vol. 1863, Columbia, Maryland, Oct. 2015, p. 2035.

[3] N. Bosanac, A. D. Cox, K. C. Howell, and D. C. Folta, "Trajectory Design for a Cislunar CubeSat Leveraging Dynamical Systems Techniques: The Lunar IceCube Mission," *Acta Astronaut.*, Vol. 144, Mar. 2018, pp. 283–296.

[4] C. Conley, "Low Energy Transit Orbits in the Restricted Three-Body Problem," *SIAM Rev. Soc. ind. Appl. Math*, Vol. 16, 1968, pp. 732–746.

[5] W. S. Koon, M. W. Lo, J. E. Marsden, and S. D. Ross, "Low Energy Transfer to the Moon," *Celest. Mech. Dyn. Astron.*, Vol. 81, 2001, pp. 63–73.

[6] G. Gómez, W. Koon, M. Lo, J. Marsden, J. Masdemont, and S. Ross, "Connecting orbits and invariant manifolds in the spatial restricted three-body problem," *Nonlinearity*, Vol. 17, No. 5, 2004, pp. 1571–1606.

[7] G. Mingotti, F. Topputo, and F. Bernelli-Zazzera, "Low-Energy, Low-Thrust Transfers to the Moon," *Celest. Mech. Dyn. Astron.*, Vol. 105, 2009, pp. 61–74.

[8] R. Anderson and M. Lo, "Role of Invariant Manifolds in Low-Thrust Trajectory Design," *J. Guid. Control Dyn.*, Vol. 32, Nov. 2009, pp. 1921–1930.

[9] A. Petropoulous and J. Sims, "A Review of Some Exact Solutions to the Planar Equations of Motion of a Thrusting Spacecraft," *2nd International Symposium on Low Thrust Trajectories*, Toulouse, France, June 2002.

[10] D. Grebow, M. Ozimek, and K. Howell, "Design of Optimal Low-Thrust Lunar Pole-Sitter Missions," *J. Astronaut. Sci.*, Vol. 58, Jan. 2011, pp. 55–79.

[11] A. Moore, S. Ober-Blöbaum, and J. Marsden, "Trajectory Design Combining Invariant Manifolds with Discrete Mechanics and Optimal Control," *J. Guid. Control Dyn.*, Vol. 35, Sept. 2012, pp. 1507–1525.

[12] A. Das and K. Howell, "Solar Sail Transfers from Earth to the Lunar Vicinity in the Circular Restricted Problem," *AAS/AIAA Astrodynamics Specialist Conference*, Vail, Colorado, Aug. 2015.

[13] V. Szebehely, *Theory of Orbits: The Restricted Problem of Three Bodies*. New York: Academic Press, 1967.

[14] M. Rayman, P. Varghese, D. Lehman, and L. Livesay, "Results From the Deep Space 1 Technology Validation Mission," *International Astronautical Congress, Session IAA.11.2: Small Planetary Missions*, Amsterdam, The Netherlands, 1999.

[15] H. Kuninaka, K. Nishiyama, Y. Shimizu, I. Funaki, and H. Koixumi, "Hayabusa Asteroid Explorer Powered by Ion Engines on the way to Earth," *31st International Electric Propulsion Conference*, University of Michigan, Ann Arbor, Michigan, Sept. 2009.

[16] C. Russel and C. Raymond, *The Dawn Mission to Minor Planets 4 Vesta and 1 Ceres*. Berlin: Springer, 2012.

[17] A. D. Cox, K. C. Howell, and D. C. Folta, "Dynamical Structures in a Low-Thrust, Multi-Body Model with Applications to Trajectory Design," *Celest. Mech. Dyn. Astron.*, Vol. 131, No. 12, 2019. Available Online.

[18] W. S. Koon, M. W. Lo, J. E. Marsden, and S. D. Ross, *Dynamical Systems, the Three-Body Problem and Space Mission Design*. New York: Springer, 2011.

[19] M. E. Paskowitz and D. J. Scheeres, "Robust capture and transfer trajectories for planetary satellite orbiters," *J. Guid. Control Dyn.*, Vol. 29, No. 2, 2006, pp. 342–353.

[20] D. C. Davis and K. C. Howell, "Characterization of trajectories near the smaller primary in the restricted problem for applications," *J. Guid. Control Dyn.*, Vol. 35, Jan. 2012, pp. 116–128.

[21] K. Howell, D. Davis, and A. Haapala, "Application of Periapse Maps for the Design of Trajectories Near the Smaller Primary in Multi-Body Regimes," *Mathematical Probl. Eng.*, Vol. 2012, 2012, pp. 1–22.

[22] T. Swenson, M. W. Lo, B. Anderson, and T. Gordordo, "The Topology of Transport Through Planar Lyapunov Orbits," *AIAA SciTech Forum*, Kissimmee, Florida, Jan. 2018.